



**HAL**  
open science

## **Yield drag in a two-dimensional foam flow around a circular obstacle: Effect of fluid fraction**

Christophe Raufaste, Benjamin Dollet, Simon Cox, Yi Jiang, François Graner

► **To cite this version:**

Christophe Raufaste, Benjamin Dollet, Simon Cox, Yi Jiang, François Graner. Yield drag in a two-dimensional foam flow around a circular obstacle: Effect of fluid fraction. 2006. hal-00090531v1

**HAL Id: hal-00090531**

**<https://hal.science/hal-00090531v1>**

Preprint submitted on 31 Aug 2006 (v1), last revised 6 Jul 2007 (v4)

**HAL** is a multi-disciplinary open access archive for the deposit and dissemination of scientific research documents, whether they are published or not. The documents may come from teaching and research institutions in France or abroad, or from public or private research centers.

L'archive ouverte pluridisciplinaire **HAL**, est destinée au dépôt et à la diffusion de documents scientifiques de niveau recherche, publiés ou non, émanant des établissements d'enseignement et de recherche français ou étrangers, des laboratoires publics ou privés.

# Yield drag in a two-dimensional foam flow around a circular obstacle: Effect of fluid fraction

Christophe Raufaste,<sup>1,\*</sup> Benjamin Dollet,<sup>1,†</sup> Simon Cox,<sup>2</sup> Yi Jiang,<sup>3</sup> and François Graner<sup>1</sup>

<sup>1</sup>*Laboratoire de Spectrométrie Physique, BP 87, 38402 St Martin d'Hères Cedex, France<sup>‡</sup>*

<sup>2</sup>*Institute of Mathematical and Physical Sciences,  
University of Wales Aberystwyth, SY23 3BZ, UK*

<sup>3</sup>*Theoretical Division, Los Alamos National Laboratory, Los Alamos, NM 87545, USA*

(Dated: August 31, 2006)

We study the two-dimensional flow of foams around a circular obstacle within a long channel. In experiments, we confine the foam between liquid and glass surfaces. In simulations, we use a deterministic software, the Surface Evolver, for bubble details; and a stochastic one, the extended Potts model, for statistics. We vary the fluid fraction in both experiments and simulations and determine the yield drag of the foam. We find that it is linear over a large range of the ratio of obstacle to bubble sizes, and is independent of the channel width over a large range. Fluid fraction, on the other hand, has a strong effect on the yield drag; at low fluid fraction the yield drag increases strongly with decreasing fluid fraction. We discuss and interpret this dependence on fluid fraction.

## I. INTRODUCTION

Multiphase materials such as colloids, emulsions, polymer or surfactant solutions, wet granular systems and suspensions of deformable objects like red blood cells are characterized by a complex mechanical behaviour [1], due to the interaction of their constitutive entities. The concentration is one of the key parameters which control the rheology, determining especially the transition from liquid-like to solid-like properties [2].

Amongst these complex fluids, liquid foams provide a convenient model experimental system for laboratory studies of the interplay between structure, concentration and rheology. This is because the bubbles which constitute the foam's internal structure can be easily visualised and manipulated. The mechanical behaviour of foams is very diverse: they appear elastic, plastic or viscous depending on the deformation and velocity gradient [3, 4].

A liquid foam consists of gas bubbles separated by a connected network of liquid boundaries. This

liquid phase occupies a fraction  $\Phi$  of the volume of the foam. The “dry foam” limit, when  $\Phi$  tends to zero, corresponds to polyhedral bubbles separated by thin walls. It is associated with a divergence of certain contributions to the viscous dissipation [5]. However, the foam's non-dissipative properties (such as surface energy [6], shear modulus or yield stress [7, 8]) usually tend to a regular, finite limit when the fluid fraction  $\Phi$  tends to zero.

The “yield drag”  $F_Y$  is the minimal force observed when there exists (or, equivalently, required to create) a movement of the foam relative to an obstacle [9]. It is a global, geometry-dependent quantity directly measurable in experiments and in practical applications of foams, for instance when a foam flows through a porous medium [10], or when one introduces an object into a foam (analogous to sticking one's finger into shaving cream). The total yield drag  $F_Y^t$  arises from the low-velocity limit (in which viscous dissipation is neglected) of two contributions,  $F^p$  due to the pressure inside the bubbles and  $F^n$  due to the network of bubble walls (i.e., soap films with surface tension):

$$F_Y^t = F_Y^p + F_Y^n. \quad (1)$$

Here we consider the network contribution  $F_Y^n$  and show how it is affected by the liquid content of the

\*Address for correspondence: craufast@ujf-grenoble.fr

†*present address*: Physics of Fluids, University of Twente, The Netherlands

‡UMR 5588 CNRS and Université Joseph Fourier.

foam.

We consider a single layer of bubbles, to facilitate preparation and analysis of experiments, as well as numerical and analytical modelling [11]. Section II presents (quasi-2D) experiments in which the foam flows around a fixed circular obstacle within a long channel: this is the historical experiment of Stokes, already adapted to foams both in 2D [9, 12] and in 3D [13, 14, 15]. We compare them with truly 2D simulations using two different software packages (Section III). The simulation methods allow easy variation of the geometrical parameters such as bubble, obstacle and channel size and better control of bubble area. Section IV presents our results: we show that the yield drag displays the expected dependence with the bubble, obstacle and channel size, and increases when the fluid fraction  $\Phi$  decreases. The discussion in Section V emphasises that taking into account the effect of fluid fraction allows all data to be plotted on a single master-curve and that the simulation results are consistent with those from experiments.

## II. EXPERIMENTAL METHODS

### A. Foam channels

Our bulk soap solution is de-ionised water with 1% Teepol, a commercial dish-washing liquid. Its surface tension, measured with the oscillating bubble method, is  $\gamma = 26.1 \pm 0.2 \text{ mN m}^{-1}$ , and its kinematic viscosity, measured with a capillary viscometer, is  $1.06 \pm 0.04 \text{ mm}^2 \text{ s}^{-1}$ .

The experimental set-up [9] confines the foam between the surface of water and a glass lid (hereafter called “liquid-glass” [16]). A 1 m long,  $w_c = 10 \text{ cm}$  wide tank is filled with soap solution, leaving below the top glass lid a free space of thickness  $h$  which we can adjust. At its centre is a circular obstacle of diameter  $d_0 = 3$  or  $4.8 \text{ cm}$  (Fig. 1). At the entrance to the channel, nitrogen is blown at a computer-controlled flow rate, which varies between 5 and 500  $\text{ml min}^{-1}$ . A typical value of the average velocity is  $3 \text{ mm s}^{-1}$ , for a 3.5 mm thickness and a flow rate of

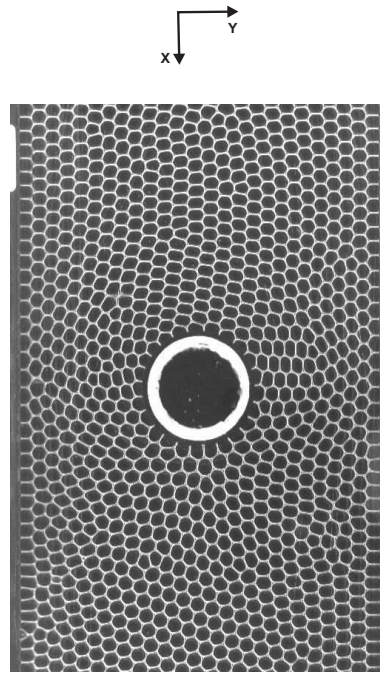


FIG. 1: Image of the experiment, with the foam confined between liquid and glass and flowing from top to bottom. Foam thickness  $h = 4.5 \text{ mm}$ ; bubble area  $A = 16 \text{ mm}^2$ ; mean velocity  $v = 5.6 \text{ mm s}^{-1}$ ; effective fluid fraction  $\Phi = 0.06$ .

$50 \text{ ml min}^{-1}$ .

The resulting foam consists of a horizontal monolayer of bubbles. It exits freely at atmospheric pressure at the open end of the channel,  $P = P_{atm}$ . In the absence of the obstacle, it yields a two-dimensional plug flow. With the obstacle present, the flow remains two-dimensional (even if the foam itself is not exactly 2D [16]): there is no vertical component of the velocity.

Due to the presence of the obstacle, there is a velocity gradient. There are many bubble rearrangements (so called “T1s” or neighbour-swapping events): two three-fold vertices contact, merge and re-separate. We observe well-separated T1s; that is, between two T1s, there is enough time for the foam to relax to an equilibrium state. The present flow is slow enough that results presented below do not depend on the velocity, and comparison with quasi-static calculations and simulations makes sense. The bubble walls meet the solid boundaries of the foam (glass plate, lateral channel walls, obstacle itself) at

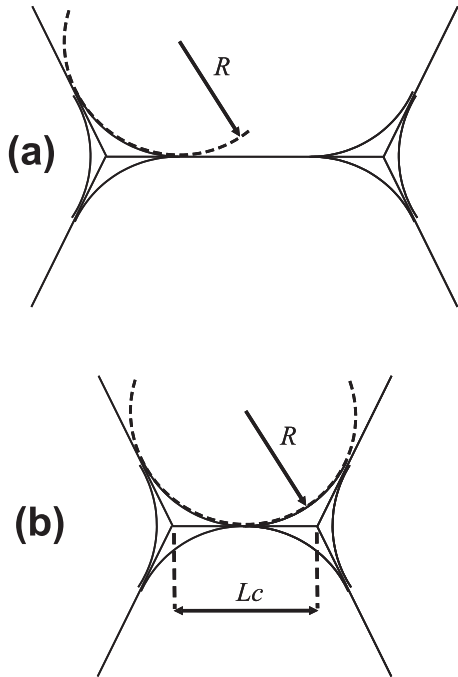


FIG. 2: Picture of two adjacent three-fold vertices with Plateau borders. (a) We apply the decoration theorem [20] to model a wet foam. The liquid is present only at the vertices, and (assuming here straight or nearly-straight walls) the uniformity of pressure  $P$  inside bubbles enforces each gas/liquid interface to have the same radius of curvature,  $R$ . (b) Critical position of the vertices just before the “T1” neighbour-swapping event. It defines the cut-off wall length  $L_c$ .

a  $90^\circ$  angle, due to the left-right symmetry [17].

The surface density of bubbles is  $1/A$ , where  $A$  is the average bubble area (including its walls). The foam is monodisperse: the area variation at the channel entrance is less than 5%. The average area is fixed at a value ranging from  $0.121 \text{ cm}^2$  to  $0.393 \text{ cm}^2$ ; most experiments have  $A = 0.160 \text{ cm}^2$ . Despite the low velocity, and hence the long transit time, we do not detect neither bubble coalescence nor coarsening. The effect of foam ageing on rheology [18, 19] is thus negligible.

## B. Fluid fraction

### 1. Fluid fraction of ideal 2D foams

In an ideal 2D foam, a Plateau border is a triangle with concave edges of radius  $R$  which match tangentially three straight lines meeting at  $120^\circ$  (Fig. 2). The area of a Plateau border is  $(\sqrt{3} - \frac{\pi}{2}) R^2$  [3].

The fluid fraction  $\Phi$  is defined as:

$$A_g = A(1 - \Phi), \quad (2)$$

where  $A_g$  is the area occupied by the gas. Thus, for a honeycomb array of bubbles:

$$\Phi = \left(2\sqrt{3} - \pi\right) \frac{R^2}{A}. \quad (3)$$

For a disordered foam, bubbles have a variable number  $n$  of sides, and eq. (3) is no longer exact. However, eq. (3) comes from the number of Plateau borders per bubble: it is linear in  $n$ , and thus involves the average  $\bar{n}$  over the foam. Since  $\bar{n} \approx 6$  in a large 2D foam [3], eq. (3) holds even for a disordered foam.

A T1 is triggered when the distance between these vertices becomes smaller than a cut-off wall length  $L_c$ , which increases with  $R$ , and thus with  $\Phi$ . To make this observation more quantitative, one possible convention to define  $L_c$  is the condition that two vertices touch (Fig. 2):

$$\frac{R}{\sqrt{3}} = \frac{L_c}{2}, \quad (4)$$

so that, together with eq. (3):

$$\Phi = \frac{3}{2} \left(\sqrt{3} - \frac{\pi}{2}\right) \frac{L_c^2}{A} \approx 0.242 \frac{L_c^2}{A}. \quad (5)$$

At given  $A$ , the physical information conveyed by  $R$ ,  $\Phi$  or  $L_c$  is the same. For comparison between different experiments or simulations, we prefer to use  $\Phi$ , which is dimensionless and intuitive.

For an ideal honeycomb lattice under homogeneous shear, all vertices merge at the same time and the hexagons become circular when  $L_c$  equals the side-length of the hexagons. This corresponds to  $\Phi = 0.091$  [7], and the honeycomb lattice loses its rigidity (vanishing shear modulus) [20].

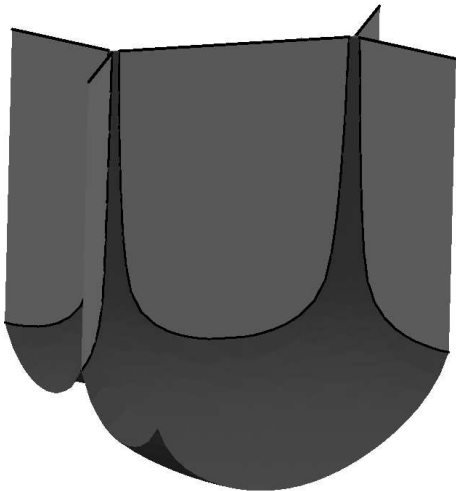


FIG. 3: Shape of a bubble of area  $16.0 \text{ mm}^2$ , and of volume  $\mathcal{V} = 16.0 \times 3.5 \text{ mm}^3$ , calculated with the Surface Evolver. To reproduce the experiment, we enforce the hexagonal symmetry and include the buoyancy. For simplicity, the junction between lateral faces and the top plate is assumed to be orthogonal.

### 2. Fluid fraction in the foam channel

In the experiment, the bubble shapes, and hence the fluid fraction  $\Phi$ , are determined by the liquid-glass distance  $h$ :  $\Phi$  decreases when the thickness  $h$  of the foam increases. It is thus easy to vary  $\Phi$ . Fig. (1) shows a foam thickness of 4.5 mm; beyond this thickness, the bubbles undergo a three-dimensional instability and the foam is no longer a monolayer [21]. At the other extreme, below 2 mm, the bubbles are circular and separated: both the foam's 2D shear modulus and the yield drag vanish.

While we observe that it is easy to vary  $\Phi$ , its definition is ambiguous [11, 16], due to the 3D shape of bubbles (Fig. 3). Throughout this paper, to establish a correspondence between the triggering of TIs in experiments, simulations and analytical expressions, we define an *effective* 2D fluid fraction.

We binarize all images using the same threshold level, and determine the surface fraction occupied by the white pixels. Since the 3D meniscus (Fig. 3) considerably expands the bubble wall thickness, this significantly overestimates  $\Phi$ . We rescale the data (we divide them by 4) so that the observed

and expected values of the rigidity loss coincide. We find  $\Phi \simeq 0.11(1 - 0.1 h)$ , where  $h$  is in mm, and an uncertainty around  $\pm 0.01$ .

## C. Force measurements

### 1. Total yield drag

The obstacle floats just below the top glass surface and is free to move, without solid friction. However, it is linked to a fixed base through a calibrated elastic fibre. We track the obstacle displacement from its position at rest using a CCD camera which images the foam flow from above. We thus measure the force exerted by the flowing foam on the obstacle (precision better than 0.1 mN) [9].

We check that the lift (spanwise component of the resultant force) is consistently zero, within fluctuations, as expected by symmetry (data not shown). After a transient, the total drag  $F^t$  (streamwise component of the resultant force) fluctuates around a steady value: we record the average and standard deviation of these steady flow data. The extrapolation to the low velocity limit (or zero-velocity intercept) of the force-velocity curve defines the yield drag  $F_Y^t$ . It is independent of the bulk solution viscosity [22], and increases with the obstacle to bubble size ratio [9].

### 2. Network contribution to the yield drag

We measure  $F_Y^n$  as follows. Each bubble wall in contact with the obstacle pulls it with a force equal to its line tension  $\lambda$ . The elastic contribution of the wall network to the drag is then the vectorial sum of all these individual forces, which all have the same modulus  $\lambda$ . As mentioned above, in a quasi-static flow each wall touches the obstacle at  $90^\circ$  angle. Thus it suffices to find the contact points between bubble walls and the obstacle, sum vectorially all outward normal vectors to the obstacle at these contact points (which is easy to determine for a circular obstacle), and multiply by  $\lambda$ . If the downstream geometry of the foam was the same as that

upstream, the drag would be zero. Since bubbles are squashed upstream and stretched downstream, the up/downstream asymmetry means that there are more bubble walls pulling the obstacle downstream, and we measure a downstream elastic contribution to the drag. To facilitate the comparison with simulations, we report the dimensionless value  $F_Y^n/\lambda$ .

In two cases we were able to measure  $\lambda$  directly by preparing a single wall pulling on the obstacle. For a thickness  $h = 4.0$  mm, we find  $\lambda = 0.44$  mN; for  $h = 4.5$  mm,  $\lambda = 0.49$  mN. We thus extrapolate to lower thicknesses as  $\lambda \approx 0.11 h$ .

### III. SIMULATIONS

#### A. Deterministic simulations (the Surface Evolver)

The Surface Evolver [23, 24] offers the possibility to reach a true quasi-static limit, that is a succession of exact equilibrium states, through a deterministic (conjugate-gradient) minimisation of the foam's energy. It yields precise details of the foam structure, including the pressure  $P$  in each bubble. We can thus separately compute  $F_Y^p$  and  $F_Y^n$ .

##### 1. Preparation of the foam

We use a mode in which all bubble walls are represented as circular arcs. The Surface Evolver lets these circular arcs evolve in order to minimise the total perimeter (equivalent to the energy, up to the prefactor  $\lambda$ ). It enforces the constraint that bubble areas  $A$  remain fixed and determines the corresponding Lagrange multipliers, namely each bubble's pressure  $P$ . Since we can freely choose the units, we call them "cm" and use bubble size  $A = 0.16$  or  $0.353$  cm<sup>2</sup>, channel width  $w_c = 10$  cm, and obstacle diameters  $d_0 = 1.5, 3$  and  $4.8$  cm, to reproduce actual experiments.

The lateral sides of the channel are rigid and do not interact with the foam, ensuring free-slip boundary conditions for the flow. We adopt a periodic boundary condition in the direction of motion: bub-

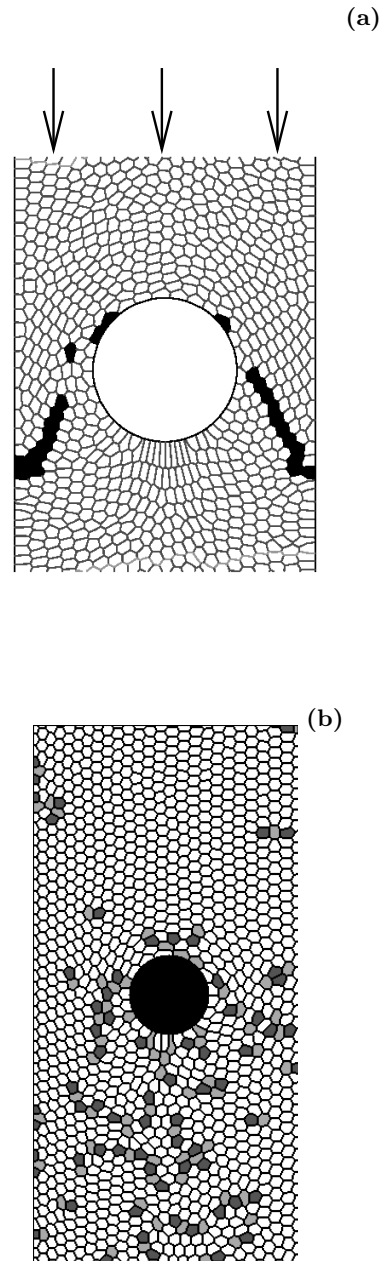


FIG. 4: Images of simulated foam flow. The  $x$ -axis is parallel to the flow along the channel, with periodic boundary conditions (exiting bubbles re-enter); axis  $y$  is spanwise, with free-slip rigid boundary conditions on either side of the channel. (a) Surface Evolver. The image shows the whole simulation domain of 750 bubbles; the shaded bubbles started in a horizontal line. Here  $d_0 = 4.8$  cm,  $A = 0.16$  cm<sup>2</sup>,  $w_c = 10$  cm,  $L_c = 0.05$  cm and therefore  $\Phi = 0.0037$ . (b) Potts model. The image shows the simulated channel's full width (except for a few pixels) of 256 pix and half the length. This is a dry foam with  $d_0 = 74$  pix,  $A = 100$  pix<sup>2</sup> and  $\Phi = 0.01$ . Bubbles coloured in white are without topological defect: 6-sided bulk bubbles, or 5-sided bubbles touching a lateral wall or the obstacle [6]. Bubbles with fewer neighbours are in dark grey, bubbles with more neighbours in light grey.

bles that exit at the end of the channel are fed back into the entrance of the channel. We stop the simulation when each bubble has passed the obstacle no more than once.

We begin with a rectangular lattice of  $30 \times 25$  monodisperse bubbles of area slightly larger than the required area  $A$ . We randomly perturb this lattice so that all the unstable four-fold vertices decay into pairs of three-fold vertices and the whole foam structure relaxes towards equilibrium. We then choose one bubble to be the circular obstacle, by slowly increasing its area to the required value (and correspondingly reducing the bubble areas to  $A$ ) and constraining its edges to lie on a circle. The centre of the circular obstacle is then moved to the centre of the channel and the structure again relaxed to equilibrium.

## 2. Simulation of the flow

With the obstacle in the desired location and the foam close to equilibrium, we start the quasi-static iteration procedure. This requires that we move the foam past the obstacle, in a direction which we denote by  $x$ ; the difficulty is in doing this with the periodic boundary conditions without fixing any vertices or bubble shapes. Our method is to choose a continuous line of consecutive bubble walls from one side of the channel to the other. Joining this to a line at  $x = 0$  with lines along the channel walls defines a plane region with a certain area. At each iteration we choose a convenient line of consecutive walls, and increment the area of the region formed by a small amount  $dA$  (equal to  $0.05 \text{ cm}^2$  in all simulations), resulting in a slight movement of a line of films without modifications of bubble areas. The total perimeter of the structure is then reduced until it converges to a constant value (Fig. 4a), so that measurements can be performed.

We have double-precision values for the network geometry. We measure the network contribution  $F_Y^n$  to the yield drag as in experiments (section II C 2). It is the sum of the unit vectors of the bubble wall with one end attached to the obstacle, expressed in

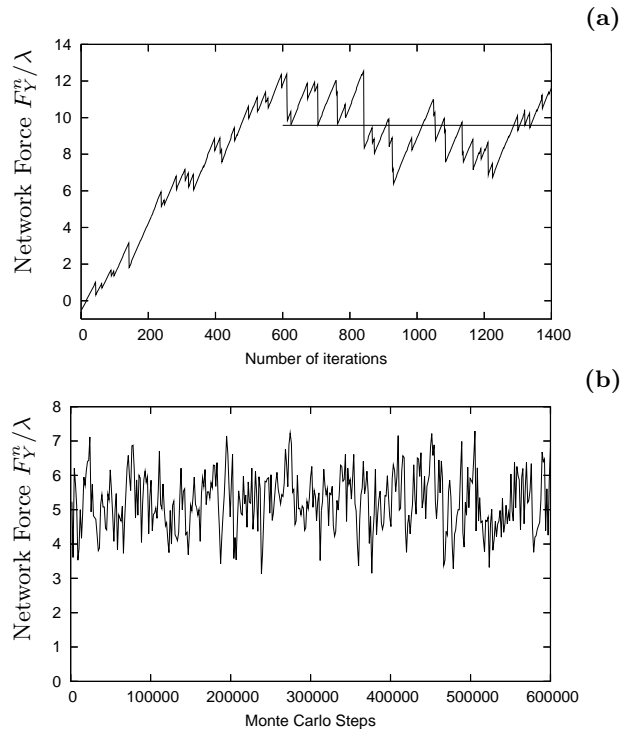


FIG. 5: The network force  $F_Y^n$  (expressed in units of the line tension  $\lambda$ ) measured in simulations *versus* time. (a) Surface Evolver data plotted every iteration step;  $d_0 = 4.8 \text{ cm}$ ,  $A = 0.16 \text{ cm}^2$  and  $L_c = 0.05 \text{ cm}$ . The plateau value is  $F_Y^n = 9.6 \pm 1.4$ . (b) Potts model data plotted every 1500 Monte Carlo Steps;  $d_0 = 74 \text{ pix}$ ,  $A = 100 \text{ pix}^2$ ,  $\Phi = 0.01$ . The plateau value is  $F_Y^n = 5.4 \pm 1.1$ .

units of the line tension (hence as a dimensionless number). Here too, we check that the lift is consistently zero within fluctuations (data not shown).

With the area increment  $dA = 0.05 \text{ cm}^2$ , the transient lasts for about 600 steps (Fig. 5a). This is comparable to but still smaller than the total simulation time that is reasonably accessible. After this transient, the drag fluctuates around a steady value. Such fluctuations recall the stress drops observed in Couette experiments for disordered foams [25, 26]; they are both linked to the rearrangements of the bubbles. We record the average and standard deviation of these plateau (steady-flow) data for a total of 1500 iterations. To validate the choice of our simulation size, we checked once that the drag forces are the same with more bubbles in the direction of flow (1250 bubbles instead of 750), although the transient is longer.

Each simulation takes about 35 hours on a Pen-

tium IV 3.20 GHz processor: typically one iteration per minute (depending on the number of bubbles and on the liquid fraction), plus a several hour build-up to the initial structure (inflating the obstacle).

### 3. Cut-off wall length and effective fluid fraction

The Surface Evolver requires to specify the cut-off wall length  $L_c$  at which two three-fold vertices are allowed to contact, merge and re-separate. This mimics the effect of liquid in the foam (Fig. 2) and defines an effective fluid fraction in simulations (eq. 5). We choose  $L_c$  of the order of 0.1 cm or slightly smaller, reaching  $\Phi = 0.0015, 0.0037, 0.0061$  and 0.015.

At very small values of  $\Phi < 6 \cdot 10^{-6}$ , films behind the obstacle would get very stretched and lead to numerical problems. Attempting larger values of  $\Phi > 0.015$  leads to poor convergence in the Surface Evolver and would require that we simulate the actual geometry of the liquid in the vertices (including 4-fold vertices).

## B. Stochastic simulations (Potts Model)

To simulate a larger number of bubbles, the Potts model adapted for foam rheology [27] also minimises the same energy, but stochastically (Monte-Carlo), drastically increasing the simulation speed. It thus provides more statistics on  $F_Y^n$  and allows greater variation of the geometrical parameters.

### 1. Principle of the Potts Model

The Potts model is derived from a large- $Q$  Potts model run at zero temperature, a model widely used to model grains in crystals [28]. It has been also applied to different domains of foam physics, including rheology, by enforcing the conservation of bubble size and applying an external force [27].

We consider a 2D square lattice. Each site  $i$  has an integer index  $\sigma_i$ . The  $k^{th}$  bubble is defined as the domain consisting of all sites with the same index value  $\sigma_i = k$ . Thus bubbles tile the plane without

gaps or overlaps. The evolution is driven by the minimisation of a total energy (strictly speaking, it is a Hamiltonian), with three contributions:

$$\mathcal{H} = \sum_{i,j \text{ neighbours}} [1 - \delta(\sigma_i, \sigma_j)] + \chi \sum_{\text{bubbles } k} (A_k - A_k^t)^2 + b \sum_{\text{sites } i} x_i. \quad (6)$$

The first term represents the contribution of the surface energy of interfaces between bubbles. Minimising this term leads to perimeter minimisation. Here  $\delta$  is the Kronecker symbol :  $1 - \delta$  is equal to 1 if the neighbouring sites  $i, j$  belong to different bubbles ( $\sigma_i \neq \sigma_j$ ); else it equals zero. The prefactor has been set to one without loss of generality. It determines the effective line tension, which is of order unity.

The second term keeps each bubble area  $A_k$  (the number of sites with the same index) close to its predefined target value  $A_k^t$ . Here  $\chi$  is the compressibility, which we choose to be high enough to keep bubble areas constant within a few pixels. The balance between this term and the preceding one simulates a foam relaxing towards mechanical equilibrium.

The third term is a bias term that describes an energy gradient, hence a homogeneous external force field. Here  $b$  is the bias intensity and  $x$  the site's coordinate along the flow. Without obstacle, the resulting velocity profile would be a plug flow.

We use a Metropolis algorithm to evolve the foam: we randomly select a site at a bubble boundary, change its index to the value of a neighbour if, and only if, this decreases the total energy (eq. 6). Several independent changes are tried successively; a Monte Carlo Step (MCS) is defined conventionally as a number of tries equal to the total number of lattice sites.

### 2. Simulation of the flow

As for the Surface Evolver (section III A 1), we choose a periodic boundary condition in the direction of flow and free-slip rigid boundary conditions on the channel sides. To ensure that it does not affect the steady-state measurements presented be-



low, the total channel length is  $4w_c$ , out of which only  $2w_c$  are used for measurements and are shown on Fig. (4b).

To match the experiments, we choose  $16 \leq d_0 \leq 148$  pix,  $64 \leq A \leq 400$  pix<sup>2</sup> and  $64 < w_c < 512$  pix. Initially, we insert a rigid round obstacle in the centre of the channel, and let a perfectly ordered foam (honeycomb pattern) flow in. We then switch off the bias term by setting  $b = 0$ , and relax the foam to ensure that the bubbles recover their (near) equilibrium state. We then switch the bias on again. We use the smallest bias  $b$  for which the foam flows, which is constant and independent of parameters such as bubble diameter.

The foam has reached the stationary state at the end of this preparation. When we switch the bias on again, we begin the measurements, performed at intervals of 1500 MCS (during which a bubble moves a few pixels).

We measure the network contribution to the drag using the same method as in the experiments and Surface Evolver simulations. It fluctuates around a steady value: we record the average and standard deviation of these plateau (steady-flow) data (Fig. 5b). We run each simulation for a total of 600,000 MCS, during which a bubble passes completely through the channel but no bubble passes the obstacle twice. One simulation takes about 12 hours on a Pentium IV 2.8 GHz processor.

### 3. Cut-off wall length and effective fluid fraction

In the Potts model, the discretisation due to the lattice has two main effects.

First, there is an unavoidable residual anisotropy of the line tension, typically a few percent [29]: it does not seem to affect the results presented below. To reduce the line tension anisotropy due to the lattice, we choose to evaluate the energy with the fourth nearest neighbour interactions [29].

Second, the lattice affects the boundaries: they are smooth if we choose a large bubble area  $A$ , at the expense of a longer computation time. The exact choice of  $A$  usually does not fundamentally affect the

results. However, we will now see that the present simulations require some attention.

The cut-off distance  $L_c$  at which two vertices can merge should be typically of the order of the pixel size on the lattice, but its exact value is difficult to define. For simplicity (and also because it yields a reasonable agreement with experiments), we assume  $L_c \approx 2$  pix. Eq. (5) thus defines an effective fluid fraction  $\Phi \approx 0.242 \times 4/A \approx A^{-1}$ . The simulated range  $64 \text{ pix}^2 \leq A \leq 400 \text{ pix}^2$  corresponds to  $0.0025 < \Phi < 0.015$ . Decreasing  $\Phi$  would require a longer computation time.

## IV. RESULTS

Both experiments and both simulations present similar images (Figs. 1, 4) and a consistent picture.

The drag force is positive (downstream), due to both the network and the pressure contributions. The Surface Evolver (data not shown) indicates that  $F_Y^p$  and  $F_Y^n$  are of the same sign and same order of magnitude, as has already been observed [24]. Experiments display the same qualitative trend (data not shown).

There are *a priori* four lengths in this problem: the channel width  $w_c$ , the obstacle diameter  $d_0$ , the bubble size  $\sqrt{A}$ ; and either the Plateau border radius  $R$  (in experiments), or the cut-off length  $L_c$  (in simulations). As far as we can tell, it is safe to assume that the channel length (if long enough) is irrelevant here. These four lengths can be reduced to three dimensionless parameters. We now present the results using:  $d_0/w_c$  which characterises the flow geometry;  $d_0/\sqrt{A}$  which describes the foam-obstacle interaction; and  $\Phi$  or  $L_c^2/A$  which characterises the threshold for T1 rearrangements.

### A. Effect of obstacle to channel size ratio

Potts model simulations indicate that the network yield drag is independent of the channel width  $w_c$  (Fig. 6a), until the obstacle (or the distance between the obstacle and the channel side [24]) is comparable to one bubble diameter.

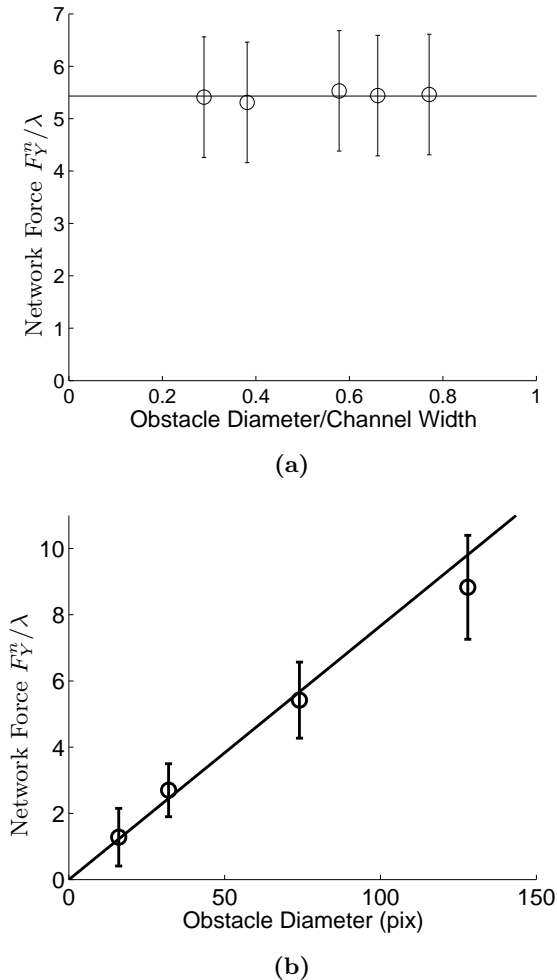


FIG. 6: Network contribution to the yield drag  $F_Y^n$  (expressed in unit of  $\lambda$ ), measured in Potts model simulations,  $A = 100 \text{ pix}^2$  ( $\Phi = 0.01$ ). (a)  $F_Y^n$  versus  $w_c$ , for  $d_0 = 74 \text{ pix}$ ; the solid line is the average (value 5.43). (b)  $F_Y^n$  versus  $d_0$ , for  $w_c = 256 \text{ pix}$ ; the solid line is a linear fit with zero intercept,  $F_Y^n = 0.77 d_0 / \sqrt{A}$ .

In 2D, elastic and hydrodynamic interactions are often logarithmic in distance, in which case the channel width would play a role. The weak dependence in  $d_0/w_c$  that we find characterises the yielding behaviour of the foam, which means that only a small region near the obstacle is affected by the flow [14]. Nonetheless, the zone where the obstacle influences the flow is larger in 2D [30] than in 3D [14].

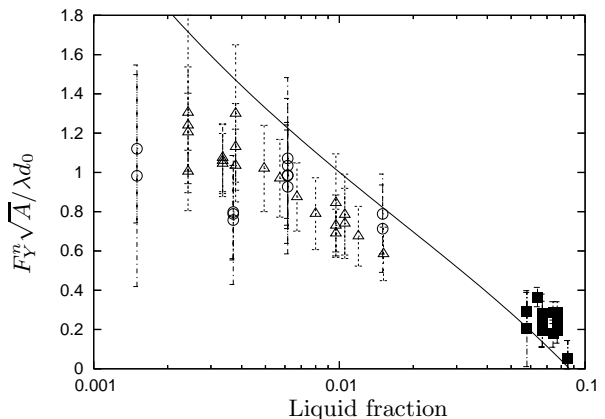


FIG. 7: The network contribution to the yield drag  $F_Y^n$ , rescaled by  $\lambda d_0 / \sqrt{A}$ , is plotted versus the effective fluid fraction  $\Phi$  defined in eq. (5), in the range  $10^{-3} < \Phi < 10^{-1}$ . Bars indicate the standard deviation of the force fluctuations in time around the plateau value. Experiments (■), Surface Evolver (○) and Potts model (△) data lie close to the solid line denoting the analytical model, from eq. (7). Note the semi-log scale.

### B. Effect of obstacle to bubble size ratio

Potts model simulations indicate that the network yield drag increases linearly with the obstacle size  $d_0$  (Fig. 6b). This is consistent with the force scaling as  $d_0 / \sqrt{A}$ , also suggested by the available Surface Evolver data, as well as by experimental measurements of the total force that show the role of the obstacle’s spanwise dimension (“leading edge”) [9]. Note that most elastic properties of a foam scale like  $1/\sqrt{A}$  [3]. In fact, when  $A$  increases, the density of bubbles and of bubble walls decreases, and so does the foam elastic modulus (it would eventually vanish if there was only one large bubble left).

### C. Effect of fluid fraction

We need to separate the effects of foam geometry,  $d_0 / \sqrt{A}$ , from those of fluid fraction. We thus rescale the network contribution to the yield drag  $F_Y^n$  by  $d_0 / \sqrt{A}$ , and plot all our data as a function of the effective fluid fraction  $\Phi$ . All the data, from both experiments and simulations, fall on the same master-curve (Fig. 7). This is the main result of the

present paper.

## V. DISCUSSION

### A. Model

The effect of the fluid fraction on the network drag can be understood as follows. A bubble of area  $A$  detaches from the obstacle when its width is of order  $L_c$ , and thus its length is of order  $A/L_c$ . When  $\Phi$  decreases,  $L_c$  decreases too. Bubbles stretch more downstream, and more bubbles pack behind the obstacle. The number of bubble walls pulling the obstacle downstream increases; simultaneously, the number of walls upstream decreases. This larger up/downstream asymmetry results in an increase in the resulting drag  $F_Y^n$ . The contribution from the network (or bubble walls) increases as their number per unit length along the obstacle boundary, namely  $L_c^{-1}$ , and thus scales like  $\sqrt{\Phi}$ .

However, the length of the region on which stretched bubbles act decreases, and the divergence in  $\sqrt{\Phi}$  is in fact softened by a geometrical factor. As shown in the Appendix, we can estimate this factor by integrating the bubble wall contribution around the obstacle. When  $\Phi$  increases,  $F_Y^n$  decreases; it vanishes for  $\Phi = 0.086$ . This is close to the rigidity loss value, namely 0.091. Eq. (17) is plotted in Fig. (7), without adjustable parameters.

The three sets of data agree in the range  $10^{-3} < \Phi < 10^{-1}$ , and the model shows qualitative agreement. This suggests we have obtained a coherent picture, where the model captures the essence of the physics, over two decades of fluid fraction.

### B. Consequences of the scaling

In the limit of low  $\Phi$ , the development of the above argument indicates that  $F_Y^n$  increases according to

$$F_Y^n = \frac{0.516}{\Phi^{1/4}} \frac{\lambda d_0}{\sqrt{A}}. \quad (7)$$

In simulations, this scaling has a surprising consequence: the network drag changes if we multiply by

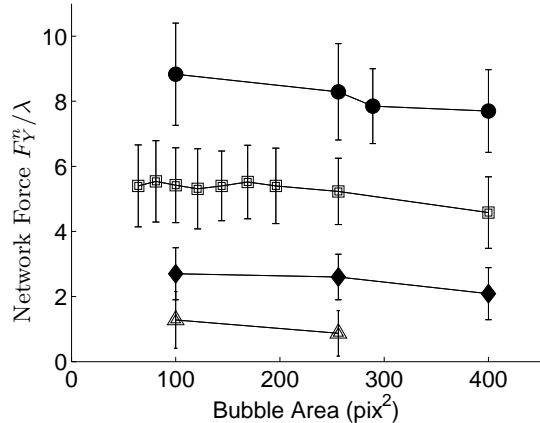


FIG. 8: Opposite effects in simulations of  $F_Y^n$  (here with Potts model). When  $A/L_c^2$  increases, both  $d_0/\sqrt{A}$  and  $\Phi$  decrease, but their effects balance each other (eq. 7), and  $F_Y^n$  barely varies. Obstacle diameter  $d_0$  equals to 16 ( $\Delta$ ), 32 ( $\blacklozenge$ ), 74 ( $\square$ ) and 128 ( $\bullet$ ).

the same prefactor the bubble, obstacle and channel sizes expressed in units of the cut-off length.

Conversely, increasing only  $A$  at fixed  $L_c$  simultaneously decreases both  $d_0/\sqrt{A}$  and  $\Phi$ ; this has two opposing effects, the former decreasing  $F_Y^n$ , the latter increasing it, resulting in an almost constant  $F_Y^n$  (Fig. 8).

### C. Saturation at low $\Phi$

Surface Evolver simulations allow us to probe the range  $10^{-5} < \Phi < 10^{-3}$ . They indicate that the force saturates below  $\Phi \sim 10^{-3}$ , in agreement with preliminary experiments of a foam confined between glass plates.

Direct observation of simulation images of very dry foams (Fig. 9) confirms that the up/downstream asymmetry is around 10 bubbles, roughly independent of liquid fraction.

The model seems to correctly describe the squashing and stretching of bubble shapes. However, the interpolation between both extreme values assumes a phenomenological expression (eq. 11), which seems too crude at low  $\Phi$ . In fact, packing many narrow bubbles around the trailing edge of the obstacle is energetically unfavourable, since the bub-

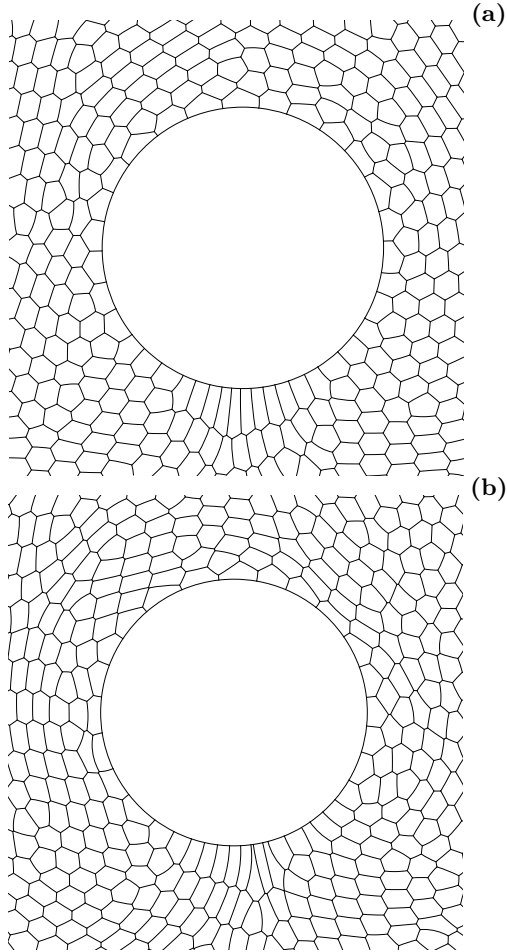


FIG. 9: Surface Evolver simulation of a very dry foam: zoom around the obstacle. (a)  $\Phi = 3.7 \cdot 10^{-3}$ ; (b)  $\Phi = 6 \cdot 10^{-6}$ . Here  $d_0 = 4.8$  cm,  $A = 0.16$  cm<sup>2</sup>,  $w_c = 10$  cm.

bles become highly anisotropic (Fig. 9b).

## VI. CONCLUSION

To summarise, we investigate the two-dimensional flow of a foam around a circular obstacle, within a long channel. Our deterministic (Surface Evolver) and stochastic (Potts model) simulations, as well as our model and experiments, complement and validate each other.

The yield drag is defined as the low-velocity limit of the interaction force between an obstacle and a flowing foam. The network contribution scales as the obstacle to bubble diameter ratio, as long as this ratio is larger than unity, and is almost independent of the channel width. It increases (because more and more stretched bubbles accumulate behind

the obstacle) as a power law when the liquid fraction contained in the foam decreases to  $10^{-3}$ , then saturates.

Its dependence with fluid fraction is well characterized. It is very different from that of local intrinsic properties such as the yield stress or shear modulus. Such observation suggests that it will be difficult to deduce one quantity from the other. This should be kept in mind in future simulations, and has to be taken into account when modelling the foam behaviour. In fact, the deformation of bubbles around the obstacle is non-trivial and difficult to model.

Although the volume of a given bubble is constant in the experiments, we can estimate the pressure contribution to the yield drag since the glass-liquid set-up has a special property: when the pressure inside a bubble increases, the thickness between the glass and liquid increases, stretching the bubble in the vertical direction. Thus its area projected on the horizontal glass lid decreases and each bubble thus acts as a pressure sensor. We observe pressure-driven variations of bubble area (especially near the obstacle) up to  $\pm 10\%$  around the area at the channel entrance. This is small enough not to perturb the flow itself and large enough to measure each bubble's pressure  $P$  [30]. Knowing  $P$  in each bubble neighbouring the obstacle allows us to obtain  $F_Y^p$ , and these values will be compared with Surface Evolver predictions in a further paper.

Future perspectives include the generalisation of the present understanding to different situations, including extension to 3D [13, 14], which should not present fundamental differences with the present 2D flow (especially since the external friction on the glass plate [31] does not seem dominant here). It is apparently applicable to other obstacle shapes like an ellipse [32].

## Acknowledgements

We gratefully acknowledge the help of Steven Thomas with Potts model simulations. We thank Isabelle Cantat for stimulating discussions, and emphasising the differences between yield drag and

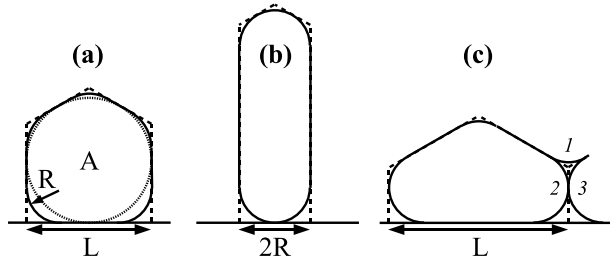


FIG. 10: Model configuration of the bubbles in contact with the obstacle. (a) Equilibrium configuration: the dashed line represents a polygonal bubble at  $\Phi = 0$ , the dotted line is a circular bubble at  $\Phi = \Phi_{\max}$ , and the plain line represents the intermediate case ( $0 < \Phi < \Phi_{\max}$ ), with straight edges and curved triangular vertices. (b) Configuration at the limit of detachment: two neighbouring vertices on the boundary of the obstacle come into contact. (c) Configuration at the limit of attachment of a new bubble. There is a first vertex between bubbles 2, 3 and the obstacle on one hand; and a second vertex between bubbles 1, 2 and 3. When they come in contact, bubble 1 attaches to the obstacle.

yield stress. CR thanks LANL and SC thanks LSP for hospitality. YJ is supported by US DOE under contract W-7405-ENG-36, SC's visit to Grenoble by the Ulysses exchange program. Part of this work was performed during the FRIT workshop [11].

#### Appendix: Variation of $F_Y^n$ with the cut-off length

We consider here only the bubbles touching the obstacle, and the contribution of their walls to the yield drag. We assume that the foam is bidimensional and monodisperse, and that  $P$  is the same for each bubble: bubble walls are straight, all Plateau borders have the same curvature radius  $R$ . We assume the obstacle is much larger than the bubbles ( $\sqrt{A} \ll d_0$ ) so that we can neglect its curvature at the bubble scale. This approximation could in principle affect the bubbles upstream, which share a long edge with the obstacle. However, it should not affect much the bubbles downstream, which are the main contributors to the drag.

#### A. Geometry

To model a wet foam, we apply the decoration theorem [20]: the liquid is present only at the vertices which decorate an ideally dry foam. For a bubble touching the obstacle, we note  $L$  the distance between two neighbouring vertices in contact with the obstacle (Fig. 10a).

When the foam flows, bubbles attach to the obstacle upstream, and detach from it downstream. Visual observation of both experiments (Fig. 1) and simulations (Fig. 4) indicate that bubbles are flattened along the obstacle at the leading side of the obstacle, and that they progressively stretch streamwise at the trailing side.

$L$  reaches its minimum value  $L_c$  downstream, where bubbles detach. There, two neighbouring (decorated) vertices come in contact, and  $L$  equals the cut-off length  $2R$  (Fig. 10b).

On the other hand, upstream, for a new bubble to attach to the obstacle, two bubbles must detach through the configuration of Fig. (10c). In this case, a vertex between three bubbles merges with one between two bubbles and the wall. The cut-off length is different, and rather equals  $(1 + 1/\sqrt{3})R$ . This geometrically determines that the maximum bubble width  $L_{\max}$  obeys:

$$A = \left(1 + \frac{1}{\sqrt{3}}\right) RL_{\max} + \frac{L_{\max}^2}{4\sqrt{3}}. \quad (8)$$

Inverting eq. (8) yields  $L_{\max}$ :

$$L_{\max}(A, R) = 2\sqrt{(\sqrt{3} + 1)^2 R^2 + A\sqrt{3}} - 2(\sqrt{3} + 1)R. \quad (9)$$

At low fluid fraction,  $L_{\max}$  tends to a finite value, namely  $\sqrt{4A\sqrt{3}}$ ; there is no singularity at vanishing  $R$ . Conversely, at high fluid fraction,  $L_{\max}$  varies much with  $R$ , so it is preferable to rewrite eq. (9) and determine  $R$  from the measurement of  $L_{\max}$ :

$$R(A, L_{\max}) = \left(1 + \frac{1}{\sqrt{3}}\right)^{-1} \left(\frac{A}{L_{\max}} - \frac{L_{\max}}{4\sqrt{3}}\right). \quad (10)$$

## B. Continuous assumption

We assume the shape of the bubbles varies smoothly from the configuration of Fig. (10c) upstream to that of Fig. (10b) downstream:  $2R < L < L_{\max}$ . Since the obstacle is much larger than the bubbles, we switch from discrete to continuous description of bubbles. We thus consider  $L$  as a continuous function of the ortho-radial angle  $\theta$  along the obstacle boundary. Equivalently,  $L^{-1}$  is the linear density of vertices along the obstacle boundary.

If we take  $\theta = 0$  in the downstream direction, then  $L(0) = 2R$ ,  $L(\pm\pi) = L_{\max}$ . To interpolate between these values, we assume the following phenomenological dependence, reflecting that all bubbles in the range  $|\theta| \geq \pi/2$  appear squashed against the obstacle:

$$\begin{aligned} |\theta| \leq \pi/2: \quad L(\theta) &= \left( R + \frac{1}{2}L_{\max} \right) + \\ &\quad \left( R - \frac{1}{2}L_{\max} \right) \cos 2\theta \quad (11) \\ |\theta| \geq \pi/2: \quad L(\theta) &= L_{\max}. \end{aligned}$$

Since each bubble edge exerts a pulling force of magnitude  $\lambda$  along the outward normal vector of the obstacle boundary, the network contribution to the drag is

$$F = \frac{\lambda d_0}{2} \int_{-\pi}^{\pi} \frac{\cos \theta}{L(\theta)} d\theta. \quad (12)$$

To compute this integral, we introduce two dimen-

sionless variables, both functions of  $A$  and  $R$ :

$$\varepsilon = \frac{R}{\sqrt{A}}, \quad (13)$$

$$\beta = \frac{L_{\max}}{2R}. \quad (14)$$

The physical meaning of  $\varepsilon$  is equivalent to the fluid fraction, since

$$\Phi = (2\sqrt{3} - \pi)\varepsilon^2. \quad (15)$$

On the other hand,  $\beta$  quantifies the amount of up/downstream asymmetry, that is, the squashing and stretching of bubbles. It increases when  $\Phi$  (or equivalently  $\varepsilon$ ) decreases (eq. 9):

$$\beta(\Phi) = \sqrt{(\sqrt{3} + 1)^2 + \frac{(6 - \sqrt{3}\pi)}{\Phi}} - (\sqrt{3} + 1). \quad (16)$$

When  $\Phi$  goes to zero,  $\varepsilon$  goes to zero too, and  $\beta$  diverges.

Using these variables, eq. (12) yields

$$F = \frac{\lambda d_0}{L_{\max}} \left[ \frac{\beta}{\sqrt{\beta - 1}} \arctan(\sqrt{\beta - 1}) - 1 \right]. \quad (17)$$

At high fluid fraction, the force  $F$  vanishes when  $\beta = 1$ , that is (eq. 16) when:

$$\Phi = \frac{2\sqrt{3} - \pi}{2 + \sqrt{3}} = 0.086. \quad (18)$$

At low fluid fraction, we develop eq. (17) to leading order in  $\beta$  and insert the leading order term of eq. (16) to obtain eq. (7).

- 
- [1] R. G. Larson, *The Structure and Rheology of Complex Fluids*, Oxford University Press, New York (1999).
- [2] A. Saint-Jalmes, D. J. Durian, *J. Rheol.* **43**, 1411 (1999).
- [3] D. Weaire, S. Hutzler, *The physics of foams*, Oxford University Press, Oxford (1999).
- [4] R. Höhler, S. Cohen-Addad *J. Phys.: Condens. Matt.* **17**, R1041 (2005).
- [5] D.M.A. Buzza, C.-Y. D. Lu and M.E. Cates, *J. Physique II* **5**, 37 (1995).
- [6] F. Graner, Y. Jiang, E. Janiaud and C. Flament, *Phys. Rev. E* **63**:11402 (2001).
- [7] H. M. Princen, *J. Coll. Int. Sci.* **91**, 160(1983).
- [8] S. A. Khan, R. C. Armstrong, *J. Non-Newtonian Fluid Mech.* **22**, 1(1986).
- [9] B. Dollet, F. Elias, C. Quilliet, C. Raufaste, M. Aubouy, and F. Graner, *Phys. Rev. E* **71**:031403 (2005).
- [10] P. L. J. Zitha, *Transp. Porous Media* **52**, 1 (2003); S. J. Cox, S. Neethling, W. R. Rossen, W. Schleifenbaum, P. Schmidt-Wellenburg, J. J. Cilliers, *Colloids Surf. A* **245**, 143 (2004).
- [11] Workshop on Foam Rheology In Two dimensions (FRIT), Aberystwyth (UK), June 2005, [HTTP://USERS.ABER.AC.UK/SXC/FRIT.HTML](http://users.aber.ac.uk/sxc/frit.html)
- [12] M. Asipauskas, J.A. Glazier, unpublished.
- [13] S.J. Cox, M.D. Alonso, S. Hutzler and D. Weaire, *in*

- Eurofoam 2000, MIT Verlag, (Bremen, 2000), eds. P. Zitha, J. Banhart, G. Verbist, p. 282-289, proceedings of 3rd Euroconference on foams, emulsions and applications, Delft (Netherlands), june 2000.
- [14] J.R. de Bruyn, *Rheol. Acta* **44**:150 (2004).
- [15] I. Cantat, O. Pitois, *J. Phys.: Condens. Matter* **17**: S3455 (2005).
- [16] M.F. Vaz and S.J. Cox, *Phil. Mag. Letts.* **85**, 415 (2005).
- [17] This is independent of the hydrophilic or hydrophobic nature of the solid surface (which would only play a role, through the presence or absence of a wetting film, in the energy dissipation, not relevant in what follows).
- [18] A. D. Gopal, D. J. Durian, *Phys. Rev. Lett.* **91**, 188303 (2003).
- [19] S. Cohen-Addad, R. Höhler, Y. Khidas, *Phys. Rev. Lett.* **93**, 028302 (2004).
- [20] F. Bolton, D. Weaire, *Phys. Rev. Lett.* **65**, 3449 (1990).
- [21] S.J. Cox, D. Weaire, and M.F. Vaz, *Eur. Phys. J. E* **7**:311 (2002).
- [22] B. Dollet, F. Elias, C. Quilliet, A. Huillier, M. Aubouy, and F. Graner, *Coll. Surf. A* **263**:101 (2005).
- [23] K. Brakke. *Exp. Math.* **1**:141 (1992).
- [24] S.J. Cox, B. Dollet and F. Graner, *Rheol. Acta* **45**: 403 (2006).
- [25] J. Lauridsen, M. Twardos, M. Dennin, *Phys. Rev. Lett.* **89**, 098303 (2002).
- [26] M. Twardos and M. Dennin, *Phys. Rev. E.* **71**: 061401 (2005).
- [27] Y. Jiang, P. J. Swart, A. Saxena, M. Asipauskas, and J. A. Glazier, *Phys. Rev. E* **59**:5819 (1999).
- [28] D.J. Srolovitz, M.P. Anderson, G.S. Grest, P.S. Sahni, *Scripta Metall.* **17** 241 (1983).
- [29] E. A. Holm, J. A. Glazier, D. J. Srolovitz, G. S. Grest, *Phys. Rev. A* **43**:2662 (1991).
- [30] B. Dollet, F. Graner, preprint (2006), physics/0606170.
- [31] D. Weaire, E. Janiaud, S. Hutzler, *Phys. Rev. Lett.* **97**:0338302 (2006).
- [32] B. Dollet, M. Durth, F. Graner, *Phys. Rev. E* **73** 061404 (2006).